Eur. Phys. J. Plus (2024) 139:247
https://doi.org/10.1140/epjp/s13360-024-05032-2

THE EUROPEAN PHYSICAL JOURNAL PLUS

Regular Article

Regulation of the thermopower and ultrasound by magnetic field in manganese sulfide doped with variable-valence ions

Sergey Aplesnin[a], **Anton Kharkov, Maxim Sitnikov**

Reshetnev Siberian State University of Science and Technology, Krasnoyarsk, Russia 660037

Received: 19 November 2023 / Accepted: 21 February 2024

Abstract The effect of cation nonstoichiometry and variable-valence samarium ions on the thermoelectric and structural characteristics of manganese sulfide is studied. Nonstoichiometry leads to a change in the thermopower sign in the antiferromagnetic region in a magnetic field and a decrease in the thermopower in the paramagnetic region. It is shown that the thermopower and Nernst–Ettingshausen coefficient of samarium-substituted manganese sulfide change their signs in the vicinity of structural and electronic transitions established from the thermal expansion coefficient. A decrease in the sound attenuation in a magnetic field is found. A correlation between the temperatures of the change of the sign of the Nernst–Ettingshausen effect and the change in electrosound in a magnetic field is established and explained within the model of carrier diffusion in the phase transition region. The conductivity control by the ultrasound is demonstrated.

1 Introduction

Controlling the transport characteristics (conductivity and thermopower) of semiconductors by a magnetic field [1–3] and ultrasound [4, 5] is an urgent fundamental and applied problem. Rare-earth sulfides are thermoelectrics with an atypically high efficiency [6–8]. The growth of the thermopower under the action of a magnetic field (the longitudinal Nernst–Ettingshausen (NE) effect) observed in topological semiconductors [9–11], ferromagnetic semiconductors [12, 13], and manganites [14, 15]. The Seebeck coefficient of the MoS_2 compound at room temperature depends on the carrier density and the NE coefficient is anisotropic [16]. In Weyl semimetals with the broken inversion, but with the time-reversal symmetry supporting chiral Weyl fermions, the sign of the NE effect can change with the spin–orbit coupling in WTe_2 [17]. In electron semiconductors, the thermopower increases in a magnetic field upon scattering by acoustic phonons and decreases upon scattering by ionized impurity atoms.

The inelastic coupling between carriers and phonons is enhanced in semiconductors that contain variable-valence elements [5]. The change in valence is accompanied by a local lattice strain and a shift in the chemical potential [18–20]. In the vicinity of phase transitions, the temperature gradient will lead to a change in the electron density of states over the sample induced by the strain gradient. In europium chalcogenides $Tm_{1-x}Eu_xSe$, the valence of thulium ions changes with the increasing dopant concentration from the trivalent state at $x = 0.2$ [21] to the divalent state at $x = 0.4$, since the 4f level shifts to the bottom of the conduction band and crosses it. The valence of thulium the $Tm_{0.6}Eu_{0.4}Se$ sample increases to $Tm^{2.175+}$ upon cooling below $T < 50$ K [22].

Samarium sulfide is a variable-valence semiconductor, which passes to the metal state under a pressure of 5.6 kbar as a result of the lattice contraction and a decrease in the lattice parameter from $a = 0.597$ nm to $a = 0.569$ nm [23–25]. An analogue of an external pressure can be a chemical pressure induced at the replacement of manganese cations in the $Sm_xMn_{1-x}S$ compounds. The initial MnS and SmS sulfides have an fcc lattice; the gap in their electron excitation spectrum differs by an order of magnitude and the lattice parameter of MnS is $a = 0.521$ nm [26]. Samarium ions at the random replacement of Mn cations are subject to different chemical pressure and Sm valence fluctuations over the $Sm_xMn_{1-x}S$ sample. Upon heating, the chemical pressure on samarium ions from the side of the MnS matrix changes as a result of thermal expansion of the lattice with a thermal expansion coefficient of $2{\cdot}10^{-5}$ K^{-1} [27]. The excess charge on $Sm^{2+\delta}$ is partially compensated by holes, which causes the local electric polarization. A lowering in local symmetry upon deformation in the vicinity of samarium ions induces the anisotropy of the electric polarization and, consequently, the anisotropy of the carrier scattering by the charged region. The Coulomb scattering potential depends on the charge and chemical pressure, which can be varied by the ultrasound power. The ultrasound attenuation leads to a strain gradient and, under the flexoelectric effect, the electric polarization is induced [28]. By varying a shear strain, one can tune the potential barrier and mobility of carriers. Thus, the current and conductivity can be controlled by ultrasound. The latter can be used to establish the thermopower mechanism caused by involve of current carriers by phonons or a gradient of current carrier density.

[a] e-mail: apl@iph.krasn.ru (corresponding author)

Published online: 13 March 2024

The effect of a magnetic field on the transport characteristics can manifest itself through the induced Kondo effect. In particular, the negative compressibility of $Sm_{1-x}Y_xS$ is explained by the strong electron–lattice coupling and the Kondo effect of electrons at the 4f level [29, 30]. In this case, we can tuning a current carrier flow by the magnetic field. In addition, the compensating charge in the vicinity of samarium creates an effective *p–n* junction. In doped silicon, the current through the *p–n* junction at room temperature changes by 20–40% in a magnetic field [31–33].

The aim of this study was to consider the possibility of tuning the thermopower and electrosound by a magnetic field and regulation of the conductivity by ultrasound and to establish the thermopower mechanism by comparing the transport characteristics with electrosound.

2 Materials and methods

The $Sm_xMn_{1-x}S$ samples were grown by crystallization of sulfide powders from melt in glassy carbon crucibles and a quartz reactor in an argon atmosphere. The complete sulfidation and homogenization of the synthesized powder sulfide was ensured by annealing at 1073 K in a sulfidation atmosphere [34]. The possible formation of cation vacancies upon substitution of samarium for manganese and their impact on the transport properties were studied on a nonstoichiometric $Mn_{0.9}S$ sample. Therefore, the samarium concentration was chosen to be $x = 0.1$ for comparison with a sample with the same vacancy concentration.

The phase composition and crystal structure of the synthesized $Sm_xMn_{1-x}S$ and $Mn_{0.9}S$ samples were examined on the DRON-3 X-ray diffractometer (CuK_α radiation) at room temperature. Figure 1 shows X-ray diffraction patterns of the samples. According to the X-ray diffraction analysis, the synthesized compounds are single-phase and, similar to the initial manganese sulfide, have a NaCl-type cubic lattice.

The morphology and the qualitative and semi-quantitative elemental compositions were exploited on a Hitachi SU3500 and TM 4000 scanning electron microscopes. Elemental mapping in the wave and energy dispersion modes adequately displays the distribution of elements in a sample (Fig. 2b). The crystal structure determined in the backscatter electron mode is consistent with the X-ray diffraction data. Scanning performed on different micro-regions of the sample yielded identical results. A microphotograph of the $Sm_{0.1}Mn_{0.9}S$ sample surface (Fig. 2a) indicates the texture formation.

The coefficients of ultrasound attenuation in the $Sm_xMn_{1-x}S$ and $Mn_{0.9}S$ compounds were determined on 0.35-cm-thick rectangular samples using two piezosensors glued to the planes, one of which was a generator and the other, a receiver of ultrasonic waves. The formula used in the calculation is

$$\gamma = \frac{\ln\left(\frac{U_1}{U_2}\right)}{d} \tag{1}$$

where U_1 and U_2 are the amplitudes of the generator and receiver voltages and d is the tablet thickness (Fig. 3a). The ac voltage induced by elastic vibrations of the sample is shifted on the receiver relative to zero by U_{sh} (the longitudinal electrosound). The voltage measured perpendicular to the speed of ultrasound is hereinafter referred to as the transverse electrosound (Fig. 3b). The current and voltage induced by the ultrasound were measured on Keithley 6517 B and Keithley 3420 instruments in two configurations.

The thermopower is studied on a plane-parallel rectangular sample (Fig. 3d). A temperature difference $\Delta T = 8$ K is created along the *OZ* axis and, as a result of charge carrier transport by a heat flow from the bottom to top face of the sample, the potential difference U_T is created, which is measured on gold contacts. The magnetic field is directed perpendicular to the temperature gradient along the *OY* axis. The potential difference was measured on a Keithley 3420 instrument. The thermal expansion coefficient β was

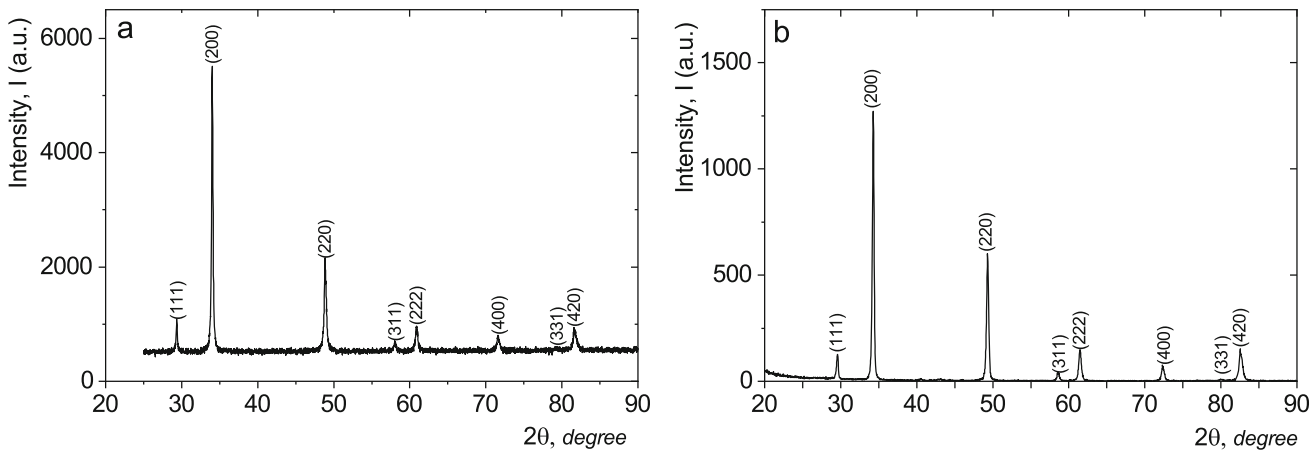

Fig. 1 X-ray diffraction patterns of samples $Sm_{0.1}Mn_{0.9}S$ (**a**) и $Mn_{0.9}S$ (**b**)

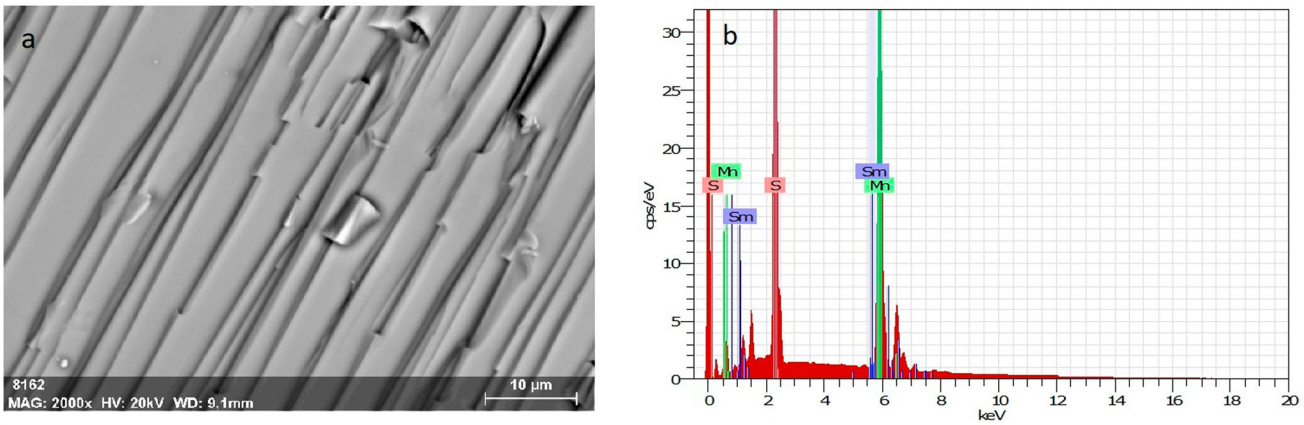

Fig. 2 Morphology (**a**) and elemental analysis (**b**) of the $Sm_xMn_{1-x}S$ sample

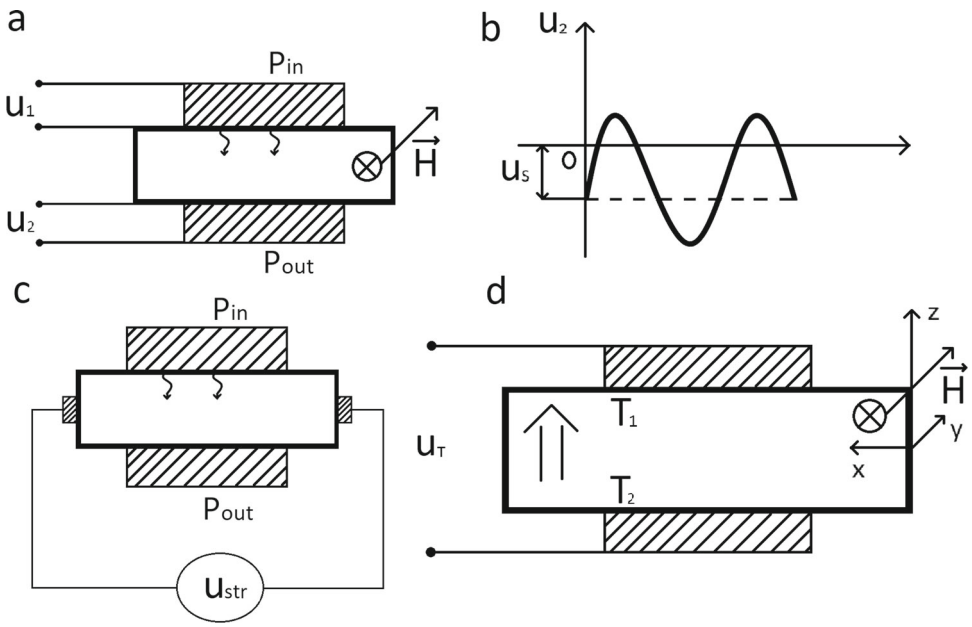

Fig. 3 Generator (P_{in}) and a receiver (P_{out}) of ultrasonic waves (**a**, **c**); the longitudinal electrosound U_s (**b**), transverse electrosound (U_{str}) (**c**); the thermopower U_T of rectangular sample (bold line) (**d**)

determined from the change in the linear dimensions (dL/L) of the sample determined from the electrical resistance of strain gauges located on the sample as $\beta = dR/dT \cdot 1/R$, where R is the electrical resistance of a strain gauge.

3 Thermopower and thermal expansion coefficient

The thermopower value is determined by thermal flows of electrons and holes. In nonstoichiometric manganese sulfide $Mn_{0.9}S$, two types of ions, Mn^{2+} and Mn^{3+}, can exist, which predetermines the existence of lattice polarons. Figure 4a shows the thermopower coefficients α without field and in a magnetic field. In the antiferromagnetic (AFM) phase, the α signs are different. The growth of the thermopower coefficient upon zero field cooling is caused by a decrease in scattering of holes by acoustic phonons. The interaction of holes with long-wave acoustic phonons describes well the experimental results $\alpha(T) \sim A/T^3$ in the low-temperature range (90–125 K) up to the temperature of the rhombohedral lattice distortion in manganese sulfide: $T = 125$ K [35, 36]. The electron flow through the cation subsystem interacts with localized spins by means of the sd coupling. In a polycrystalline antiferromagnet, the magnetic moments of sublattices are canted in an external magnetic field and the magnetization along the field is created. Upon heating, the AFM susceptibility increases due to an increase in the magnon density, which enhances the electron scattering by magnons and determines the $\alpha(T)$ dependence. The thermopower coefficient in a magnetic field is negative and proportional to the magnetization, which is described in the mean-field approximation by the power function $\text{abs}(\alpha(T)) = A(1–T/T_N)^{1/2}$. In the paramagnetic region, $\alpha(T)$ decreases in a magnetic field due to the partial localization of carriers. In a magnetic field, the blurred thermopower maxima at $T = 245$ and 400 K shift to $T = 215$ and 465 K.

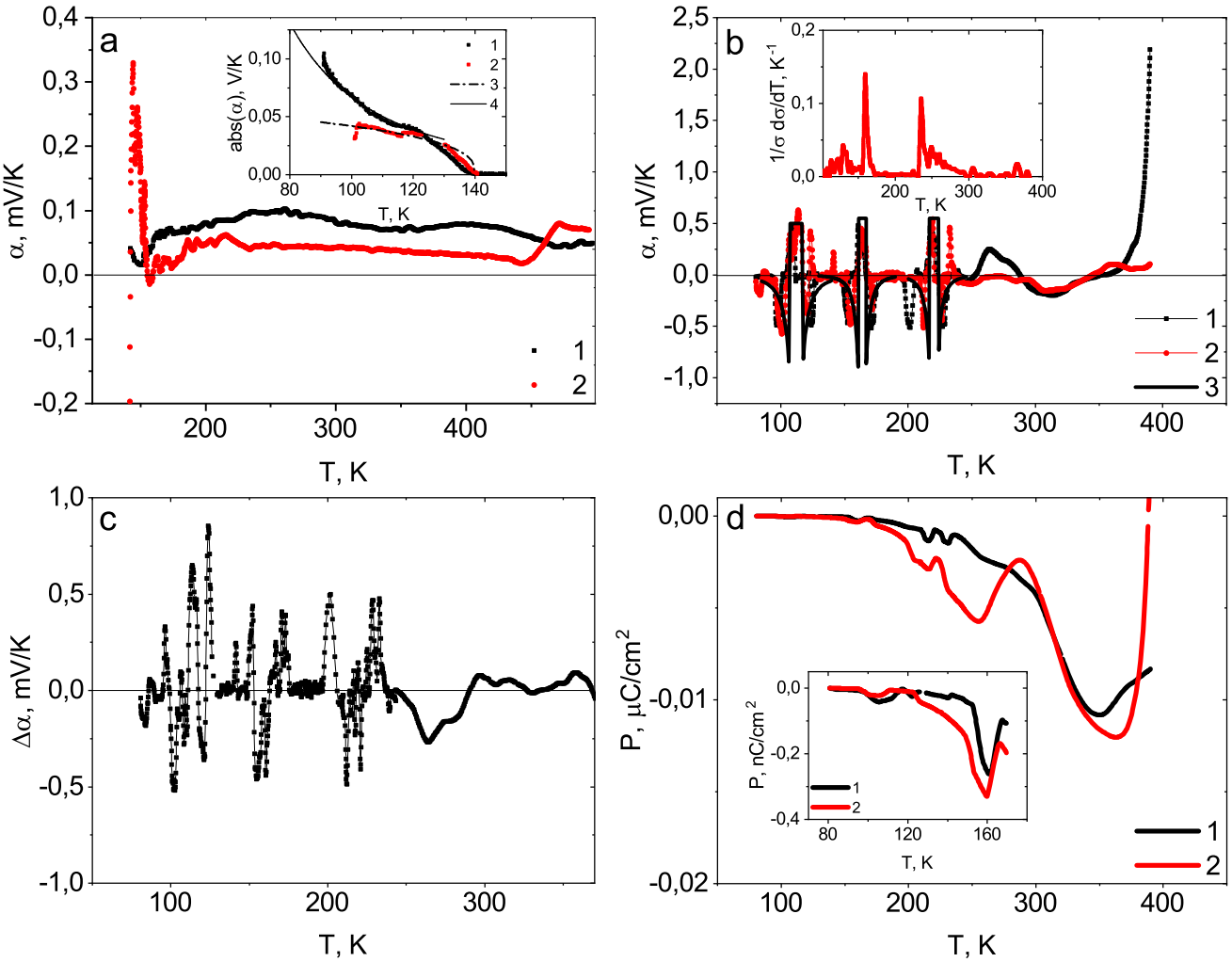

Fig. 4 Thermopower for $Mn_{0.9}S$ (**a**) and $Sm_{0.1}Mn_{0.9}S$ (**b**) without a field H = 0 (1) and in a magnetic field H = 8 kOe (2) and fitting function (3) on temperature. Insert: temperature coefficient of conductivity 1/(d/dT) for $Sm_{0.1}Mn_{0.9}S$. Longitudinal Nernst–Ettingshausen coefficient (NE) Δα = (α(H)–α(H = 0)) (**c**). Temperature dependence of electric polarization (**d**) in $Sm_{0.1}Mn_{0.9}S$ without a field H = 0 (1) and in a magnetic field H = 8 kOe (2). Insert: temperature dependence of electric polarization

Substitution of samarium for manganese in MnS qualitatively changes the temperature dependence of the thermopower coefficient. First, the thermopower decreases by more than two orders of magnitude and, second, α(T) experiences temperature oscillations in the range of $R(T)$ anomalies (Fig. 4b). Samarium ions have a variable valence and, in the temperature range of the crystal structure distortions, polar regions with a local electric polarization arise (Fig. 4d). The temperature gradient leads to a change in the polarization: $dP/dT = dP/dt\ 1/(dT/dt)$. The potential difference across the sample induced by the temperature gradient is determined by the change in the carrier density $(\Delta n_p + \Delta n_e)e/l$ along the sample length and the migration-type electric polarization. Let us estimate the induced polarization $P = \int j dt = \int \sigma E dt = \int \sigma U dT/l(dT/dt)$. In a magnetic field, the migration polarization increases at T = 100, 160, 210, 250, and 355 K due to an increase in the electron localization.

Using the temperature dependences of the thermopower, we determine the NE coefficient: (NE) Δα = abs(α(H))–abs(α(H = 0)). The appearance of electric field in the conductor in the presence of a temperature gradient ∇T in the direction, perpendicular to the magnetic field is NERNST–ETTINGSHAUZEN effect. There are transverse and longitudinal NE effects [37]. The appearance of an electric field in a semiconductor in a direction perpendicular to the magnetic field and gradient of temperature is determined as the transverse NE effect. If the temperature gradient is directed along the X axis, and the magnetic field is directed along the Z axis, then the resulting electric current parallel to the Y axis. Longitudinal NE effect consists of the appearance of an electric field in the semiconductor (differences in potentials) along the temperature gradient in the presence of a magnetic field H⊥∇T. The appearance of an additional field along ∇T arise from bending of the flow of electrons trajectory and reduce their free path length in the direction of ∇T.

In electron semiconductors, the thermopower in a magnetic field increases upon scattering by acoustic phonons and decreases upon scattering by ionized impurity atoms. In $Mn_{0.9}S$, the thermopower decreases in a field over the entire temperature range,

except for 125–140 K and $T > 470$ K. The temperature oscillations of the NE coefficient in $Sm_{0.1}Mn_{0.9}S$ are caused by the contact potential difference between the two phases and diffusion. In the single-phase state, the temperature gradient across the sample induces gradients of phonons and the density of electronic states. The energy flow from hot to cold is accompanied by a flow of charged particles:

$$j_N = D\frac{dN}{dx} \approx v\lambda\frac{dN}{dx} = \frac{v}{N}\frac{dN}{dx} \approx \frac{\tau}{m_{ef}}\frac{1}{N}\frac{dN}{dx} \tag{2}$$

where v is the velocity expressed via relaxation time τ as $v = \mu E = e\tau/m_{ef}E$. In the temperature range of the structural transition, two phases appear in the sample together with the contact potential difference $U_c = kT/e\ \ln(n_A/n_B)$, where n_A/n_B are the carrier densities in phases A and B. The sign difference between the contact and diffusion potential difference leads to a change in the thermopower sign. In the vicinity of electronic structural transitions (Tc), a change in the concentration of current carriers will lead to jumps in conductivity and to maxima of the temperature coefficient of conductivity 1/(d/dT) (inset in Fig. 4b). An increase in the relaxation time in the critical region leads to singularities in the quantities of collective transport, for example, mutual diffusion, shear and bulk viscosity [38]. The increase in relaxation time is associated with an increase in the thermal correlation length, which is determined by the power function $\tau \sim 1/(Tc - T)^z$, where z is the dynamic critical index in the three-dimensional system $Z = 3.068$ [38].When a new phase is formed, the growth of the correlation radius is cut off by the nucleus of the new phase,which we take into account in the form $A/(abs(T - Tc) + \Delta T)^z$. In the vicinity of the transition, two phases are formed in a sample with a temperature gradient ΔT. In this case, under certain conditions, the contact potential difference exceeds the potential difference created during the diffusion of current carriers. The temperature behavior of α(T) is approximated by the function:

$$\alpha = A/(abs(T - T_c) + \Delta)^z + kT_c/e\ln(n_A/n_B), \tag{3}$$

which satisfactorily describes the experimental results below room temperature with the electron concentration ratio n_A/n_B from 0.6 at T = 115 K to 0.4 at 230 K. The contact potential difference of phases A and B is Uc ≈ 3 mV in the temperature range $Tc - \Delta T/2 < T < Tc + \Delta T/2$.

For the $Mn_{0.9}S$ sample, the broad maximum of the thermal expansion coefficient and the thermopower α(T) exist in the same temperature region: 215–230 K. The maximum at $T = 167$ K is related to the orthorhombic lattice distortion in MnS [35]. The contact potential difference in the vicinity of the transition rhombic distortion–cubic structure in $Mn_{0.9}S$ is smaller than in $Sm_xMn_{1-x}S$, since samarium ions exhibit the anomalous compressibility [39] and a significant change in the carrier density in phases A and B. The valence growth leads to a decrease in the ionic radius. Figure 5b shows the thermal expansion coefficient of the $Sm_{0.1}Mn_{0.9}S$ lattice. In contrast to $Mn_{0.9}S$, the $Sm_{0.1}Mn_{0.9}S$ sample expands upon cooling below 100 K. The negative thermal expansion coefficient $\beta = -1.2\cdot10^{-4}$ K^{-1} of ruthenium oxides is explained by the feature of the crystal structure [40]. The reduction of the volume $\Delta V/V = -0.03$ in $Sm_{1-x}Y_xS$ upon heating is interpreted as the intra-atomic charge redistribution [41]. Against the background of four broad maxima, the β(T) dependence contains several peaks: at $T = 124$, 150, 167, 207, 250, and 442 K. Three β(T) peaks coincide with the maxima of the MnS thermal expansion coefficient at 125, 147, and 165 K, two of which are caused by the cubic lattice symmetry lowering. The angle of the cube vertex distortion is directly proportional to the exchange rate and inversely proportional to the elastic modulus of the crystal. A change in the Me–S–Me bond angle evokes the exchange striction of the lattice and compression at 147 K. The anomalies at 207 and 250 K are related to a displacement-type structural transition induced by rotation of octahedra in one plane and in two planes. Similar transitions were observed in oxides with the structures of perovskite [42] and stanate [43]. The broad β(T) maxima at $T = 367$ K are related to the compensation of charged $Sm^{2+\delta}$ ions and delocalization of electrons from samarium impurity ions at $T = 442$ K. Similar anomalies in the transport characteristics were observed in the $BaSnO_3$ compound [44] as a result of the localization of small-radius polarons on oxygen defects. A change in the carrier density n at the level of the chemical potential μ will lead to anomalies in the coefficient of compressibility : $1/ = d^2E/dn^2 = (dn/d\mu)^{-1}$. Let us establish the role of acoustic phonons in the entrainment of electrons in the thermopower using ultrasound.

4 Ultrasound attenuation and electrosound

We determine the entrainment of carriers by an elastic wave from the ultrasound in a magnetic field in two configurations: a voltage along the sound wave propagation (the longitudinal effect) and perpendicular to the wave (the transverse effect) in a magnetic field directed perpendicular to the ultrasound velocity vector (Fig. 3). In the AFM region, the attenuation increases and saturates with an increase in the ultrasound intensity. The ultrasound is strongly absorbed in the AFM region and, during the transition to the paramagnetic state, the absorption sharply decreases by 25%. In the temperature range of 140–280 K, the attenuation increases linearly with the intensity and, above room temperature, depends weakly on the ultrasonic power. The ultrasound attenuation is related to the interaction of an elastic wave with carriers and determined by the electron relaxation time. We make the estimation using the equation [45]:

$$\gamma = \frac{K^2}{2}\frac{\omega_C}{(v_S - \mu E)}\left[1 + \frac{\omega_C^2 v_S^2}{(v_S - \mu E)^2\omega^2}\left(1 + \frac{\omega^2}{\omega_C\omega_D}\right)\right]^{-1} \tag{4}$$

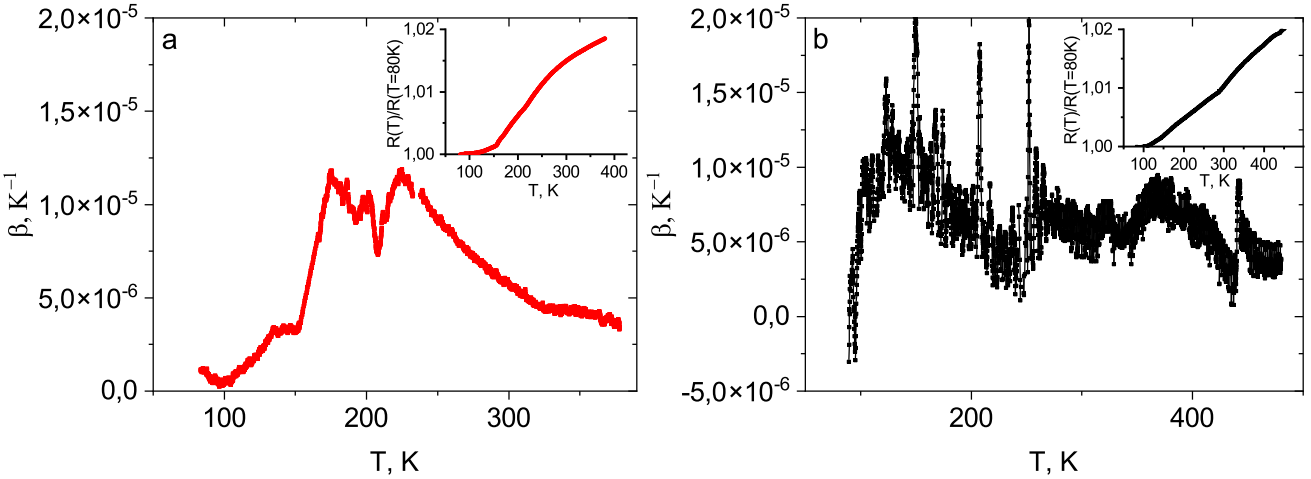

Fig. 5 Thermal expansion coefficient β for $Mn_{0.9}S$ (**a**) and $Sm_{0.1}Mn_{0.9}S$ (**b**) on temperature. Inserts: relative change in strain gauge on a sample as a function of temperature

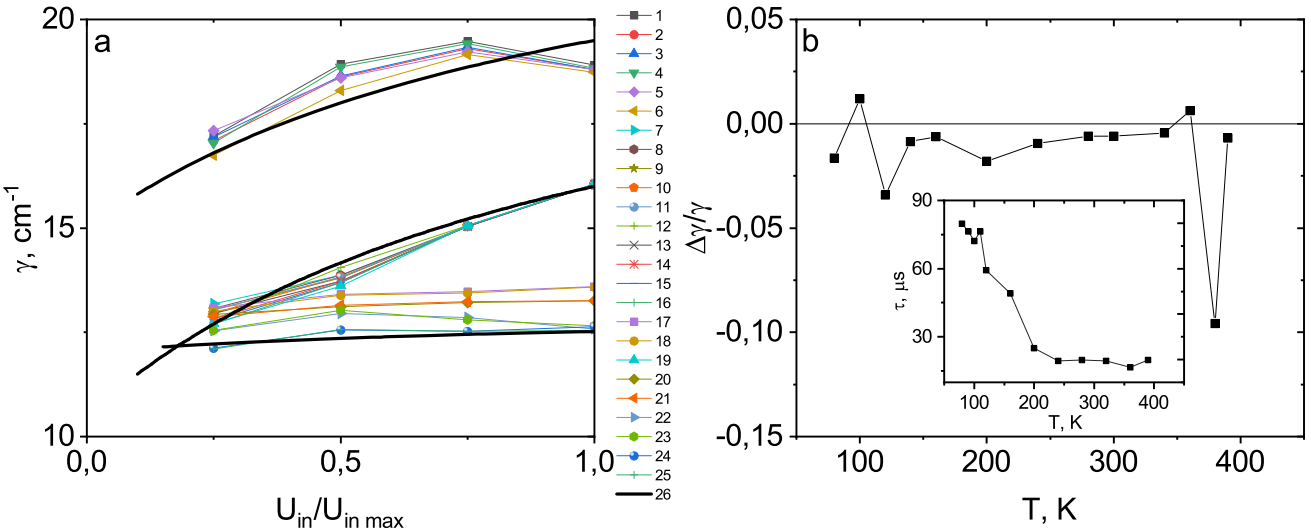

Fig. 6 Ultrasound attenuation coefficient γ (**a**) in $Sm_{0.1}Mn_{0.9}S$ from the normalized power of the sound wave without a field H = 0 (1,3,5,7,9,11,13,15,17,20,22,24) and in magnetic field H = 12 kOe (2,4,6,8,10,12,14,16,18,19,21,23,25) at fixed temperatures T = 80 K (1,2), 100 K (3,4), 120 K (5,6), 140 K (7,8), 160 K (9,10), 200 K (11,12), 240 K (13,14), 280 K (15,16), 300 K (17,18), 320 K (19), 340 K (20,21), 360 K (22,23), 390 K (24,25). Fitting functions (26) according to Eq. (4). Change in the ultrasonic attenuation coefficient (γ(H) – γ(0))/γ(0) (b) in a magnetic field H = 12 kOe. Insert: temperature dependence of relaxation time τ

where K is the electromechanical coupling coefficient, μ is the electron mobility, v_s is the speed of sound, E is the applied dc electric field, ω is the acoustic frequency, ω_C is the dielectric relaxation frequency, and ω_D is the dielectric diffusion frequency. Here, we have $\omega >> \omega_C$ and $E = 0$ and the attenuation factor has the form

$$\gamma = K^2 \frac{\omega_D}{2v_S} \frac{\frac{\omega_C}{\omega_D}}{1 + \frac{\omega_C}{\omega_D}} \tag{5}$$

The $\gamma(T)$ dependence coincides qualitatively with the carrier relaxation time determined from the impedance (inset in Fig. 6b). The relaxation time decreases by 20% during the transition from the AFM to paramagnetic state and, at $T > 200$ K, depends weakly on temperature. The time of relaxation of carriers entrained by an elastic wave depends on the sound intensity and is proportional to $(\omega_C/\omega_D) \sim U_{in}/U_{max}$. We use (5) as an approximating function. The diffusion frequency is higher than the dielectric relaxation frequency by an order of magnitude and, in an antiferromagnet, it is $\omega_D = 9 \cdot 10^4$ Hz; upon heating, it increases to $1.2 \cdot 10^5$ Hz and, above 280 K, drops. The diffusion coefficient possibly passes through a maximum.

The relative change in the coefficient $\Delta\gamma/\gamma$ of the ultrasound attenuation in a magnetic field is illustrated in Fig. 6b. The ultrasound attenuation weakens in a magnetic field, in particular, by $\Delta\gamma/\gamma = 3\%$ in the vicinity of the Néel temperature and by $\Delta\gamma/\gamma = 10\%$ around 380 K, where the electric polarization vanishes. In the range of the Néel temperature $T_N = 140$ K [46], the magnetic field

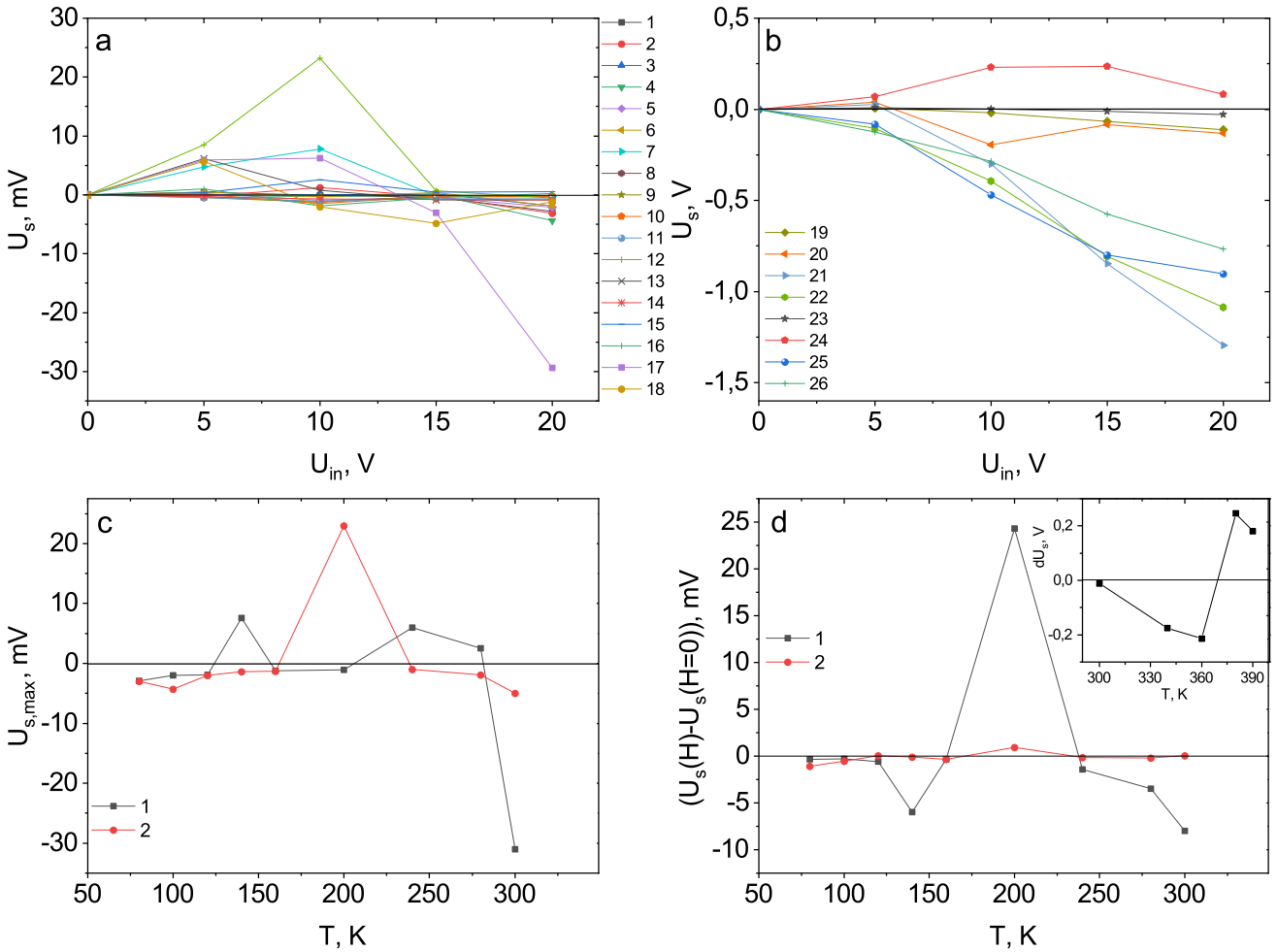

Fig. 7 Electric voltage U_s induced by ultrasound (**a**, **b**) in $Sm_{0.1}Mn_{0.9}S$ from the power of a sound wave without a field H = 0 (1,3,5,7,9,11,13,15,17,19,21,23,25) and in magnetic field H = 12 kOe (2,4,6,8,10,12,14,16,18,20,22,24,26) at fixed temperatures T = 80 K (1,2), 100 K (3,4), 120 K (5,6), 140 K (7,8), 160 K (9,10), 200 K (11,12), 240 K (13,14), 280 K (15,16), 300 K (17,18), 340 K (19,20), 360 K (21,22), 380 K (23,24), 390 K (25,26). Maximum voltage $U_{s\ max}$ at H = 0 (1), H = = 12 kOe (2) versus temperature (**c**); change in longitudinal electrosound (1) in a magnetic field H = 12 kOe, U_{in} = 10 V and longitudinal Nernst–Ettingshausen coefficient (2) versus temperature (**d**) and at temperatures above room temperature (insert)

suppresses spin fluctuations and the scattering of spin polarons weakens. In the paramagnetic range the diffusion frequency drops, which leads to a decrease in the attenuation coefficient, since electrons entrained by an acoustic wave are affected by the Lorentz force, in addition to the electric field of the wave.

Let us check our assumption by comparing the electrosound induced by a piezosensor with the thermopower. The voltage on the sample induced during propagation of the ultrasound is determined from the shift of harmonic oscillations on the output piezosensor at times of 10^{-5}–10^{-6} s (Fig. 7).

The sign of the electrosound voltage does not change with temperature at intensities higher than $U > 15$ V. At low sound intensities, the voltage sign changes from positive to negative at $T = 80$, 120, 140, 240, 280, and 300 K (Fig. 7a). Near these temperatures, the thermopower sign changes. At $T > 200$ K, the maximum value of the electrosound (Fig. 7c) exceeds the thermopower value several times.

The voltage is induced by a strain gradient created by an elastic wave. The amplitude of the longitudinal acoustic wave decreases in the sample and leads to the formation of dielectric polarization as a result of the flexoelectric effect. A similar effect was observed in germanium and silicon [45]. The flexoelectric effect can be taken into account when studying the interaction of free current carriers with the deformation field in centrosymmetric crystals. The flexoelectric effect and deformation potential provide the same energy of interaction between current carriers and the acoustic wave [45]. The lattice strain leads to a shift in the chemical potential μ and a change in the electron density N on the chemical potential, since there is a correlation between the bulk elastic modulus and chemical potential: $1/B = d\mu/dN$. The energy passes from the elastic to electron system at the periodic lattice contractions. This may be due to the anomalous compressibility of samarium ions: $= 1/V\ (dV/dP)$. As the ultrasound is intensified, near the ultrasound generator (A) the local electric polarization in the strain radius region is formed with the potential $\varphi_A > 0$. The maximum

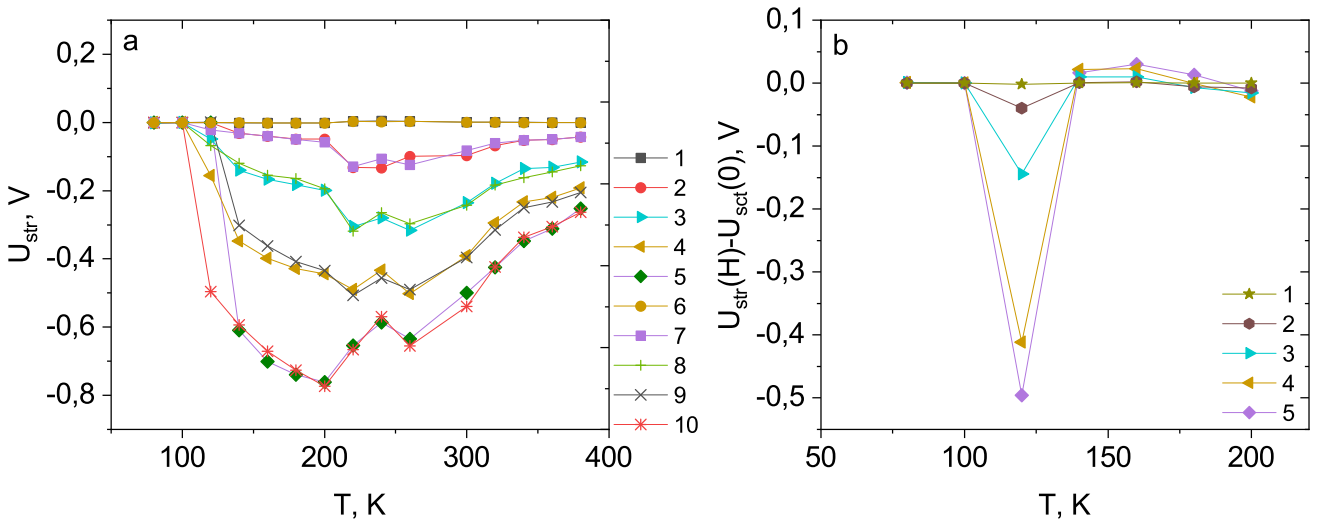

Fig. 8 Transverse voltage (Fig. 3c) generated by ultrasound in $Sm_xMn_{1-x}S$ at U_{in} = 0 V (1), 5 V (2), 10 V (3), 15 V (4), 20 V (5) without field H = 0 (1,2,3,4,5) and in a magnetic field H = 12 kOe (6,7,8,9,10) (**a**) and the change in voltage in the magnetic field (**b**) from temperature

ultrasound intensity causes the maximum deformation of potential wells with the delocalization of holes and the formation of the negative potential $\varphi_A < 0$, which changes the electric field polarity. The ultrasound-induced voltage attains its maximum at 360 K and is caused by the disappearance of the local electrical polarization.

At the maximum ultrasound intensity, the electric voltage in a magnetic field decreases due to a decrease in the diffusion of carriers and an increase in the localization time. In a magnetic field, the electrosound polarity changes with the increasing intensity at T = 120, 200, 280, 300, and 380 K, which is also consistent with the temperatures of changes in the thermopower. The relative change in the electrosound, as the thermopower in a magnetic field, oscillates with temperature (Fig. 7d).

The electric field (voltage) induced by the ultrasound and directed perpendicular to the wave propagation is shown in Fig. 8. Above the Néel temperature, the voltage increases by an order of magnitude, attains its maximum around the temperature of the displacement-type structural transition (at 220–260 K), and sharply drops at 340 K. The change in the voltage in a magnetic field around T_N = 140 K increases nonlinearly (Fig. 8b) with the ultrasound intensity and, in the range of 140–190 K, the electrosound decreases to 8% in a magnetic field. In the Néel temperature region, the electric polarization P = 0.1 μC/cm^2 is induced by the ultrasound with the colossal magnetoelectric effect: $\alpha = P/H$ = 0.09 μC/(cm^2·T). The voltages induced by the ultrasound along and perpendicular to the velocity direction differ by more than an order of magnitude. Under the action of the ultrasound, a shear strain occurs. In an elastically isotropic solid, there are two elastic moduli: the longitudinal elastic modulus and the shear modulus, which, as a rule, is an order of magnitude smaller, for example, eight times smaller in silicon and by an order of magnitude in MoS_2 [47]. As a result of the shear strain, holes are delocalized in the *xy* plane parallel to the plane of the piezosensor. Holes are entrained by transverse elastic waves and this leads to separation of the positive and localized negative charges. The growth of the transverse stress by more than an order of magnitude as compared with the longitudinal one is related to the electron–lattice coupling. The latter shifts the 5d band downward in energy, depending on the samarium ion volume V, which can be presented in the linear approximation as $E_0(V) = E_0(V_0)$–$g(V$–$V_0)$ [48].

The energy of the electron and lattice system has the form [48]:

$$E(n_c) = -[E_0(V_0) - G]n_c + \frac{1}{2\rho}n_c^2 - \left(G + \frac{g^2 V_0}{2B_0}\right)n_c^2 \tag{6}$$

where G is the electron–electron interaction parameter, ρ is the electron density of states of the 5d band, n_c is the electron density in the conduction band, B_0 is the bulk modulus of elasticity, and g is the parameter of the electron–lattice coupling. Equation (6) has a minimum at

$$n_c = \frac{E_0(V_0) - G}{\frac{1}{2\rho} - G - \frac{g^2 V_0}{2B_0}} \tag{7}$$

The account for the electron–lattice interaction leads to an increase in the carrier density. The drop of the elastic modulus, for example, the replacement of B_0 by shear modulus K will lead to an increase in the density: $\Delta n_c/n_c \sim g^2(B_0/K$–$1)$.

In the $Sm_xMn_{1-x}S$ compound, unlike a piezoelectric, the ultrasound induces a current with charge transfer through the sample. Figure 9 shows the current as a function of the ultrasound intensity and temperature. The $I(U)$ dependence is well approximated by the power function $I(P) = AU^3$ in the range of 80–240 K. The $I(T)$ dependence qualitatively coincides with the voltage up to a temperature of 340 K, above which the electric polarization vanishes. The change in the samarium ion volume is $(V - V_0)/V_0$ =

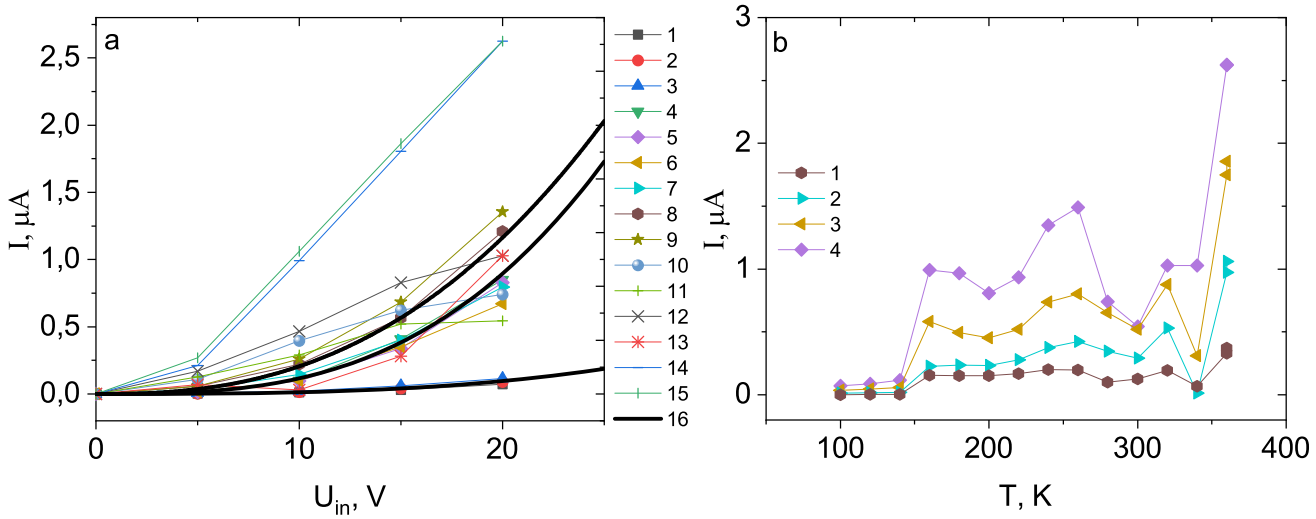

Fig. 9 Electric current induced by ultrasound, the speed of which is perpendicular to the current (**a**) in $Sm_{0.1}Mn_{0.9}S$ from the intensity of the sound wave at fixed temperatures T = 100 K (1), 120 K (2), 140 K (3), 160 K (4), 180 K (5), 200 K (6), 220 K (7), 240 K (8), 260 K (9), 280 K (10), 300 K (11), 320 K (12), 340 K (13), 360 K (14), 380 K (15), fitting functions $I = AU^3$ (16) and on temperature (**b**) at ultrasound intensities U_{in} = 5 V (1), 10 V (2), 15 V (3), 20 V (4)

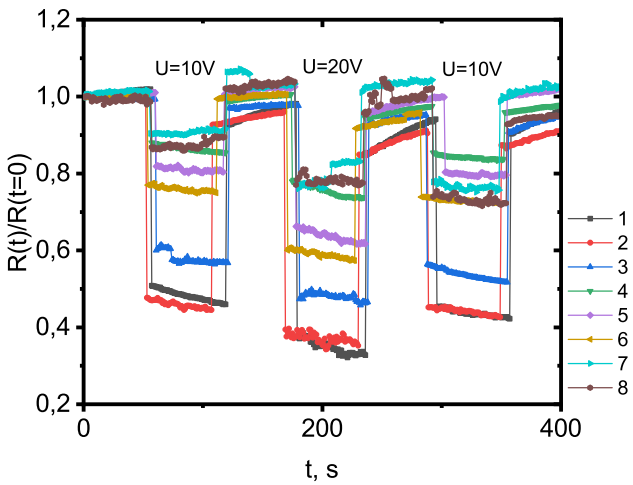

Fig. 10 Normalized resistance R(t)/R(t = 0) versus time when ultrasound is periodically turned on with U_{in} = 10 V, 20 V at temperatures T = 80 K (1), 120 K (2), 160 K (3), 200 K (4), 240 K (5), 280 K (6), 320 K (7), 360 K (8)

$[(a–a_0)/a_0]^3 = gn_s/B_0$. The linear strain induced by a piezosensor in the sample is $(a–a_0)/a_0 = kU_{in}$, where k is the electromechanical conversion factor, U_{in} is the voltage on the piezosensor, and a is the Mn–S–Sm bond length. Thus, the electric sound is $I \sim n_s \sim U_{in}{}^3$.

In the configuration with the electric current perpendicular to the speed of sound, the resistance can be tuned. Figure 10 shows the normalized resistance versus time with an interval of 1 min: U = 0, t = 0–60 s; U = 10 V, t = 61–120 s; U = 0, t = 121–180 s; U = 20 V, t = 181–240 s; U = 0, t = 241–300 s; U = 10 V, t = 301–360 s; and U = 0, t = 361–420 s. In the AFM region, the resistance decreases by a factor of more than 2. In the magnetically ordered state, the electron–lattice coupling leads to an increase in the volume and a decrease in the exchange interaction. Electrons in the AFM region self-localize with the formation of ferrons [49]. The ferron radius increases with a decrease in the exchange field and the potential barrier for electron hopping between ferrons lowers [50].

In the paramagnetic region, the potential barrier between wells decreases under the action of ultrasound and the carrier density and, consequently, the conductivity increase. At room temperature, the resistance can be varied by up to 20% with good repeatability of the results. These samples can be used as audio transistors in a wide temperature range (from 80 to 360 K).

5 Conclusions

A comparison of the transport characteristics of nonstoichiometric manganese sulfide and samarium-substituted one showed the absence of cation vacancies in $Sm_{0.1}Mn_{0.9}S$. The thermopower of nonstoichiometric manganese sulfide in the AFM region is caused by scattering of holes by acoustic phonons and, in a magnetic field, by scattering of electron by magnons. In the paramagnetic region,

the thermopower is caused by holes and decreases in a magnetic field in $Mn_{0.9}S$. In the $Sm_{0.1}Mn_{0.9}S$ sample, the thermopower oscillations with temperature in the range of structural transitions are caused by the diffusion of carriers and the contact potential difference between the phases. In a magnetic field, a shift of the thermopower maxima causes oscillations of the NE coefficient. The lattice expansion upon cooling below 100 K was found in $Sm_{0.1}Mn_{0.9}S$, in contrast to the compression observed in $Mn_{0.9}S$. A correlation between the temperatures of the maximum thermal expansion coefficient and thermopower in the $Sm_{0.1}Mn_{0.9}S$ compound was established. A change in the sign of the longitudinal electrosound below room temperature and oscillations of the thermopower and longitudinal NE coefficient in the region of the structural and electronic transitions as a result of the competition between the diffusion of carriers and the contact potential difference were found. Oscillations of the electrosound changes in a magnetic field are caused by the strain gradient and the electron–lattice coupling. The possibility of controlling the conductivity by the ultrasound in a wide temperature range was demonstrated.

Acknowledgements The study was supported by a grant from the Russian Science Foundation N 23-22-10016, the Krasnoyarsk Regional Science Foundation. The investigation of microstructural properties of the samples was carried out using equipment's (SEM and TEM) the Krasnoyarsk Regional Center of Research Equipment of Federal Research Center «Krasnoyarsk Science Center SB RAS». The authors are grateful to A.V. Shabanov for the scanning electron microscopy investigations.

Data Availability Statement The manuscript has no associated data or the data will not be deposited.

Declarations

Conflict of interest The authors declare that they have no known competing financial interests or personal relationships that could have appeared to influence the work reported in this paper.

References

1. F. Jansson, M. Wiemer et al., J. Appl. Phys. **116**, 083710 (2014). https://doi.org/10.1063/1.4894236
2. H. Takahashi, T. Akiba, A.H. Mayo et al., Phys. Rev. Mater. **6**, 054602 (2022). https://doi.org/10.1103/PhysRevMaterials.6.054602
3. K. Takiguchi, L.D. Anh, T. Chiba et al., Nat. Phys. **15**, 1134 (2019). https://doi.org/10.1038/s41567-019-0621-6
4. G. Benedek et al., J. Phys. Chem. Lett. **11**, 1927 (2020). https://doi.org/10.1021/acs.jpclett.9b03829
5. S.S. Aplesnin, M.N. Sitnikov et al., Eur. Phys. J. Plus **137**, 226 (2022). https://doi.org/10.1140/epjp/s13360-022-02432-0
6. F.F. Jaldurgam, Z. Ahmad, F. Touati, Nanomaterials **11**(4), 895 (2021). https://doi.org/10.3390/nano11040895
7. A.V. Powell, J. Appl. Phys. **126**, 100901 (2019). https://doi.org/10.1063/1.5119345
8. L.L. Zhao, X.L. Wang, F.Y. Fei et al., J. Mater. Chem. A **3**(18), 9432 (2015). https://doi.org/10.1039/c5ta01667c
9. K. Dybko, P. Pfeffer, M. Szot et al., New J. Phys. **18**, 013047 (2016). https://doi.org/10.1088/1367-2630/18/1/013047
10. Y. Tanaka, Z. Ren, T. Sato et al., Nat. Phys. **8**, 800 (2012). https://doi.org/10.1038/nphys2442
11. Y. Pan, B. He, T. Helm et al., Nat. Commun. **13**, 3909 (2022). https://doi.org/10.1038/s41467-022-31372-7
12. T.T. Lan Anh, Y.E. Ihm et al., Thin Solid Films **518**, 309 (2009). https://doi.org/10.1016/j.tsf.2009.04.051
13. V.N. Men'shov, V.V. Tugushev et al., Phys. Rev. B **83**, 035201 (2011). https://doi.org/10.1103/PhysRevB.83.035201
14. M. Jaime et al., Appl. Phys. Lett. **68**, 1576 (1996). https://doi.org/10.1063/1.116686
15. V.H. Crespi et al., Phys. Rev. B **53**, 14303 (1996). https://doi.org/10.1103/PhysRevB.53.14303
16. G. Sharma, Phys. Rev. B **98**, 075416 (2018). https://doi.org/10.1103/PhysRevB.98.075416
17. C. Zeng, S. Nandy et al., Phys. Rev. B **100**, 245102 (2019). https://doi.org/10.1103/PhysRevB.100.245102
18. O. Tschauner, Geosciences **12**(6), 246 (2022). https://doi.org/10.3390/geosciences12060246
19. A. Bakar, A. Afaq et al., Phys. B: Cond. Matt. **576**, 411715 (2020). https://doi.org/10.1016/j.physb.2019.411715
20. T. Matsuoka, H. Fujihisa, N. Hirao et al., Phys. Rev. Lett. **107**, 025501 (2011). https://doi.org/10.1103/PhysRevLett.107.025501
21. W. Reim, P. Wachter, Phys. Rev. Lett. **55**, 871 (1985). https://doi.org/10.1103/PhysRevLett.55.871
22. E. Kaldis, B. Fritzler, Prog. Sol. St. Chem. **14**, 95 (1982). https://doi.org/10.1016/0079-6786(82)90003-6
23. D. Schaller, P.G. LaBarre, T. Besara et al., Phys. Rev. Mater. **3**, 104602 (2019). https://doi.org/10.1103/PhysRevMaterials.3.104602
24. A. Sousanis, P.F. Smet, D. Poelman, Materials **10**(8), 953 (2017). https://doi.org/10.3390/ma10080953
25. K. Takenaka, D. Asai, R. Kaizu et al., Sci. Rep. **9**, 122 (2019). https://doi.org/10.1038/s41598-018-36568-w
26. S.S. Aplesnin, L.I. Ryabinkina, G.M. Abramova et al., Phys. Rev. B **71**, 125204 (2005). https://doi.org/10.1103/PhysRevB.71.125204
27. S.S. Aplesnin, O.B. Romanova, M.V. Gorev et al., J. Phys. Cond. Matt. **25**, 025802 (2013). https://doi.org/10.1088/0953-8984/25/2/025802
28. S.S. Aplesnin, A.N. Masyugin et al., JETP Lett. **110**(3), 223 (2019). https://doi.org/10.1134/S0021364019150074
29. D.G. Mazzone, M. Dzero et al., Phys. Rev. Lett. **124**, 125701 (2020). https://doi.org/10.1103/PhysRevLett.124.125701
30. I. Jarrige, A. Kotani, H. Yamaoka et al., Phys. Rev. Lett. **114**, 126401 (2015). https://doi.org/10.1103/PhysRevLett.114.126401
31. D. Yang, F. Wang, Y. Ren et al., Adv. Funct. Mater. **23**, 2918 (2013). https://doi.org/10.1002/adfm.201202695
32. C. Wan, X. Zhang, X. Gao et al., Nature **477**, 304 (2011). https://doi.org/10.1038/nature10375
33. Y. Cao, D. Yang, M. Si et al., Appl. Phys. Exp. **11**, 061304 (2018). https://doi.org/10.7567/APEX.11.061304
34. S.S. Aplesnin, L.I. Ryabinkina, O.B. Romanova et al., Phys. Sol. St. **51**(4), 698 (2009). https://doi.org/10.1134/S1063783409040076
35. O.B. Romanova, S.S. Aplesnin, M.N. Sitnikov et al., Sol. St. Commun. **364**, 115134 (2023). https://doi.org/10.1016/j.ssc.2023.115134
36. H.H. Heikens, G.A. Wiegers, C.F. van Bruggen, Sol. St. Commun. **24**, 205 (1977). https://doi.org/10.1016/0038-1098(77)91198-X
37. N.P. Gavaleshko, P.N. Gorley, P.V. Kavyuk et al., Phys. Status Solidi B **88**, 179 (1978). https://doi.org/10.1002/pssb.2220880121
38. P.C. Hohenberg, B.I. Halperin, Rev. Mod. Phys. **49**, 435 (1977). https://doi.org/10.1103/RevModPhys.49.435.S2CID122636335
39. H.A.A. Sidek, G.A. Saunders, R.N. Hampton et al., Phil. Mag. Lett. **57**(1), 49 (1988). https://doi.org/10.1080/09500838808227797
40. K. Takenaka, Y. Okamoto et al., Nat. Commun. **8**, 14102 (2017). https://doi.org/10.1038/ncomms14102
41. A. Jayaraman, P. Dernier, L.D. Longinotti, Phys. Rev. B **11**, 2783 (1975). https://doi.org/10.1103/PhysRevB.11.2783

42. K.S. Aleksandrov, A.T. Anistratov, B.V. Beznosikov, N.V. Fedoseeva, *Phase Transitions in Crystals of the Halide Compounds ABX3* (Nauka, Novosibirsk, 1981)
43. L.V. Udod, S.S. Aplesnin, M.N. Sitnikov et al., J. Alloys Comp. **804**, 281 (2019). https://doi.org/10.1016/j.jallcom.2019.07.020
44. G. Geneste, B. Amadon, M. Torrent et al., Phys. Rev. B **96**, 134123 (2017). https://doi.org/10.1103/PhysRevB.96.134123
45. A.K. Tagantsev, JETP **61**, 1246 (1985)
46. S.S. Aplesnin, O.B. Romanova et al., Phys. Stat. Sol. B **248**, 1975 (2011). https://doi.org/10.1002/pssb.201046544
47. J.L. Feldman, J. Phys. Chem. Sol. **37**, 1141 (1976). https://doi.org/10.1016/0022-3697(76)90143-8
48. D.I. Khomskii, Phys. Usp. **22**, 879 (1979). https://doi.org/10.1070/PU1979v022n11ABEH005645
49. E.L. Nagaev, Phys. Usp. **38**, 497 (1995). https://doi.org/10.1070/PU1995v038n05ABEH000085
50. M.Y. Kagan, K.I. Kugel, Phys. Usp. **44**, 553 (2001). https://doi.org/10.1070/pu2001v044n06abeh000917